

Received 3 June 2014

Accepted 11 July 2014

# Ultra-thin optical grade scCVD diamond as X-ray beam position monitor

**Kewin Desjardins,<sup>a\*</sup> Michal Pomorski<sup>b</sup> and John Morse<sup>c</sup>**

<sup>a</sup>Synchrotron SOLEIL, L'Orme des Merisiers, Saint-Aubin, 91192 Gif-sur-Yvette, France, <sup>b</sup>CEA-LIST, Diamond Sensors Laboratory, 91191 Gif-sur-Yvette, France, and <sup>c</sup>European Synchrotron Radiation Facility, 6 rue Jules Horowitz, 38043 Grenoble, France.

\*E-mail: kewin.desjardins@synchrotron-soleil.fr

Results of measurements made at the SIRIUS beamline of the SOLEIL synchrotron for a new X-ray beam position monitor based on a super-thin single crystal of diamond grown by chemical vapor deposition (CVD) are presented. This detector is a quadrant electrode design processed on a 3 µm-thick membrane obtained by argon–oxygen plasma etching the central area of a CVD-grown diamond plate of 60 µm thickness. The membrane transmits more than 50% of the incident 1.3 keV energy X-ray beam. The diamond plate was of moderate purity (~1 p.p.m. nitrogen), but the X-ray beam induced current (XBIC) measurements nevertheless showed a photo-charge collection efficiency approaching 100% for an electric field of  $2 \text{ V } \mu\text{m}^{-1}$ , corresponding to an applied bias voltage of only 6 V. XBIC mapping of the membrane showed an inhomogeneity of more than 10% across the membrane, corresponding to the measured variation in the thickness of the diamond plate before the plasma etching process. The measured XBIC signal-to-dark-current ratio of the device was greater than  $10^5$ , and the X-ray beam position resolution of the device was better than a micrometer for a 1 kHz sampling rate.

**Keywords:** ultra-thin optical-grade single-crystal CVD diamond; X-ray beam position monitor; XBIC; XBPM.

© 2014 International Union of Crystallography

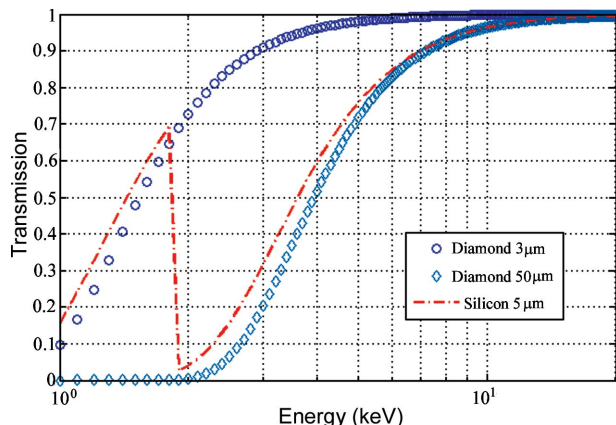
## 1. Introduction

Beamlines at third-generation synchrotron facilities are now routinely capable of focusing X-ray beams down to a few tenths of a micrometer, and a corresponding level of beam position stability is critical for many experiments. Stability requirements are even more exacting for new scanning nanoprobe beamlines with undulator source-to-sample station lengths greater than 100 m, using mirror optics that focus the X-ray beams to less than 30 nm at the sample (Somogyi *et al.*, 2011; NINA beamline at the ESRF). These beamlines may acquire experimental data with sampling times down to a millisecond during dynamic position scans over the samples (Medjoubi *et al.*, 2013). This requires fast (~1 kHz bandwidth) diagnostics to precisely monitor the instantaneous beam flux with accuracy at the percent level, and to determine the beam position with respect to the sample with a precision that is better than the focused beam size.

Existing X-ray beam position monitor (XBPM) devices are mostly based on the principle of a thin metal or other foil inserted into the beam, with detection of the resulting scattered and fluorescence X-rays from the foil. These devices do not provide a sufficiently high signal-to-noise ratio for our requirements, primarily due to the poor solid-angle efficiency

of detecting the X-rays produced by the foil. Foils of sufficient thickness to have a practical level of robustness are also too absorbing of soft X-ray beams. Examples of these systems are the now widespread foil and four photodiodes system (Alkire *et al.*, 2000), and the more recent aperture camera system (van Silfhout *et al.*, 2011). Efficient detection of all beam-intercepted photons has been achieved using silicon photodiodes fabricated with position-sensitive resistive contacts: these can be made with silicon thickness down to ~5 µm and have been successfully tested by Fuchs *et al.* (2007), although their radiation hardness and stability remain a problem. However, for X-rays at low energies, and especially just above the silicon absorption threshold at 1.8 keV, silicon devices have an unacceptable level of beam absorption. Gaseous ionization XBPMs (Schildkamp & Pradervand, 1995) can achieve good efficiency with acceptable (and easily varied) beam absorption, but compared with solid-state semiconductor devices their position response is poor owing to the typically several millimeters range of photoelectrons generated in the gas; in addition, beam-absorbing entrance and exit windows are required to contain the working gas.

XBPMs based on thin plates of polycrystalline diamond grown by chemical vapor deposition (pcCVD) and with metal surface contacts were pioneered by CEA-LIST (Bergonzo *et*

**Figure 1**

X-ray beam transmission *versus* incident-beam energy for 3  $\mu\text{m}$  and 50  $\mu\text{m}$  diamond and, for comparison, transmission for a 5  $\mu\text{m}$ -thick silicon plate.

*et al.*, 1999). Diamond plates are both mechanically robust and radiation hard, and with low X-ray beam absorption, *i.e.* a diamond plate of thickness 50  $\mu\text{m}$  has the equivalent absorption as 3  $\mu\text{m}$  of silicon (Fig. 1). The first polycrystalline diamond devices showed poor electrical charge collection, resulting in a sensitivity which only permitted their measurements in a white synchrotron beam. Furthermore, abrupt spatial variations in charge collection efficiency were observed, which correlated directly with the crystal-grain boundaries present in the material. This spatial response inhomogeneity and the lag effects in measured signal currents caused by charge trapping at grain boundaries result in pcCVD being a material of limited use for fabricating XBPMs and, in particular, for microfocused X-ray beams. Since 2002, single-crystal CVD (scCVD) diamond plates of high purity (substitutional nitrogen and boron contamination of less than 5 p.p.b.) have been commercially available from Element Six Ltd (Ascot, UK; <http://www.e6.com>). The carrier lifetimes of up to  $\sim$ 500 ns measured in this material (Isberg *et al.*, 2002; Pomorski *et al.*, 2007) result in a close to complete collection of the X-ray-beam-created photocharge, even for millimeter charge drift distances, and, when suitably contacted and electrically biased, XBPMs fabricated from this material and tested with a scanning submicrometer X-ray beam have demonstrated complete charge collection with a spatial response that is uniform at the 0.1% level on the micrometer scale when mapping areas of several  $\text{mm}^2$  (Morse *et al.*, 2007). Due to its wide bandgap (5.5 eV), the room-temperature leakage currents measured in such scCVD devices are extremely low, typically  $<\text{pA mm}^{-2}$  for operation under applied electric fields of  $\sim$ 0.5 V  $\mu\text{m}^{-1}$ . Such diamond detectors have now been made by several groups using various metal contacts (Al, Cr–Au, Pt, ...) for X-ray, high-energy particle and heavy-ion detection (Bohon *et al.*, 2010; Berdermann *et al.*, 2010). Position sensitivity can be obtained by interpolation of the current signals measured from neighboring surface contacts, and submicrometer beam position noise has been demonstrated using both electrometer and radiofrequency readout approaches (Morse *et al.*, 2010; Muller *et al.*, 2012; Desjardins

*et al.*, 2013). This work has been carried out using scCVD plates of thicknesses from 500  $\mu\text{m}$  down to  $\sim$ 40  $\mu\text{m}$ , which is the practical limit for abrasive thinning–polishing of this material, beyond which breakage of the plates during processing becomes increasingly likely. In order to satisfy the performance requirements of soft-energy ( $<5$  keV) X-ray beamlines, we began the development of ‘super thin’ XBPM devices based on free-standing scCVD diamond membranes of  $\sim$ 4  $\mu\text{m}$  thickness. Results from the X-ray beam characterization of first devices, obtained at the SIRIUS beamline of Synchrotron SOLEIL (<http://www.synchrotron-soleil.fr>), are presented here.

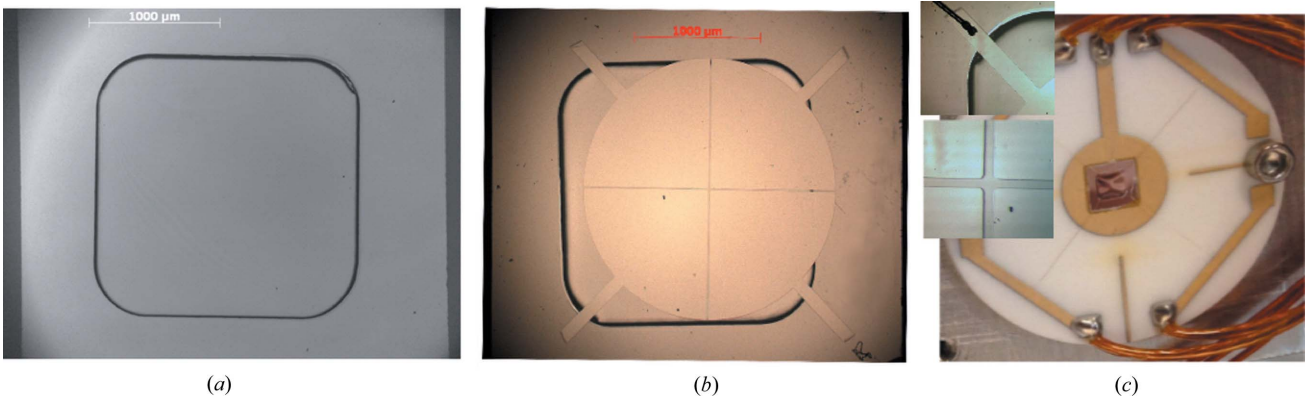
## 2. Experimental method

### 2.1. XBPM fabrication

An Element Six 3 mm  $\times$  3 mm scCVD diamond plate of [100] face orientation and initial thickness 0.3 mm was thinned and fine-scaife polished to a thickness of 60  $\mu\text{m}$ . The grade of diamond chosen has a substitutional nitrogen content of  $<1$  p.p.m., which is far above that of the higher-cost Element Six ‘electronic’ grade material (N<sub>sub</sub>s < 5 p.p.b.) which is grown slower and with fewer defects. Nitrogen is known to create a deep (2.7 eV) electron trap in diamond and the consequences of charge trapping are shown below. A polycrystalline diamond plate with a laser cut 2 mm  $\times$  2 mm hole was superposed on the scCVD plate to act as a shadow mask, and, by deep argon–oxygen plasma etching, a free-standing membrane of 3.3  $\mu\text{m}$  thickness was created in the center (Fig. 2*a*) leaving a surrounding 60  $\mu\text{m}$  ‘window frame’ support (Pomorski *et al.*, 2013). The opposite side of the detector was also Ar–O etched over its entire area to a depth of 5  $\mu\text{m}$  to remove sub-surface damage to the diamond crystal created by the previous mechanical polishing processes. After boiling-acid cleaning the etched plate, aluminium electrodes of 200 nm thickness were sputter-deposited using the photolithographic lift-off technique to create a simple four-quadrant electrode pattern with an inter-electrode gap of 10  $\mu\text{m}$  (Fig. 2*b*). The rear (deep etched) side of the plate was aluminium sputter-coated without the need for lithography, to form the opposing bias electrode. Thus processed, the detector was glued onto a metallized alumina ceramic using a UHV-conducting epoxy to provide rear-side electrical contact, and connections made to the front-side quadrant electrodes with aluminium wedge wire bonding (Fig. 2*c*).

### 2.2. XBPM model

Interaction of the X-ray beam with the diamond material generates free charge carriers (electron–hole pairs), primarily *via* the photoelectric effect. An initial energetic photoelectron multiple scatters and is thermalized within a picosecond, creating a charge cloud of a few micrometers size. The hole and electrons of this charge cloud drift apart under the influence of the applied electric field created by the externally biased surface electrodes, thus generating electric current in the external circuit. Beam-position information results from

**Figure 2**

Freestanding membrane scCVD diamond XBPM fabrication: (a) 3  $\mu\text{m}$ -thick scCVD diamond membrane surrounded by a 55  $\mu\text{m}$ -thick window frame, (b) after sputtering and lift-off lithography, showing the 200 nm-thick Al quadrant pattern, and (c) the processed detector bonded to its ceramic support ready for beamline testing.

the division of the moving charges towards or away from the four electrodes. In the present case, where the beam size is far larger than the isolation gap between the electrodes, the signal partition is essentially defined by the geometric overlap of the beam intensity with the individual quadrant electrodes. Assuming that the beam is symmetric with respect to reflection about the  $x$  and  $z$  axes, for movements of the beam that are small compared with its size, a simple linear approximation algorithm can be used to determine the beam-center coordinates as

$$\begin{aligned} X &= K_x[(I_1 + I_4) - (I_2 + I_3)]/I_0 \quad \text{and} \\ Z &= K_z[(I_3 + I_4) - (I_1 + I_2)]/I_0, \end{aligned} \quad (1)$$

where  $I_1$  to  $I_4$  denote the electrical currents of the four electrodes and  $I_0$  is the sum of all four currents; these signal currents are corrected for any measured offsets related to electrode dark currents and/or instrumentation zero offsets.  $K_x$  and  $K_z$  are scale factors corresponding to the beam displacement in the horizontal and vertical directions relative to the center of the four quadrants; these scale factors are determined experimentally by scanning the XBPM across the beam in orthogonal directions. Note that for such quadrant XBPMs, the values  $K_x$  and  $K_z$  will vary with the incident-beam size and its spatial intensity distribution (Kazovsky, 1983).

The measured current induced by the X-ray beam interaction is given by the simplified equation

$$I = q \frac{E_{\text{ph}}}{\varepsilon_p} A \varphi \frac{\mu \tau E}{L}, \quad (2)$$

where  $I$  is the total current produced by the XBPM,  $q$  is the value of the electron charge,  $E_{\text{ph}}$  is the incident-beam energy and  $\varepsilon_p = 13.25 \pm 0.5 \text{ eV}$  is the electron-hole-pair creation energy (Keister & Smedley, 2009) for X-ray absorption in diamond.  $A$  is the fraction of the beam flux  $\varphi$  that is absorbed by the photoelectric effect, and  $\mu$  and  $\tau$  are the charge carrier mobility and lifetimes, respectively, averaged over holes and electrons.  $E$  is the electric field applied between the quadrant electrodes and the rear bias electrode, and is taken to be  $U/L$ , where  $U$  is the applied bias and  $L$  is the diamond plate

thickness. This is a reasonable assumption, as we show by the data below that there was no indication of polarization effects within the diamond bulk or at surface interfaces to the metal contacts. The charge collection efficiency (CCE), *i.e.* the fraction of the total charge which contributes to the measured signal current, is accounted for by the term  $\mu \tau E/L$ . Compton scattering in the diamond plate can be ignored, as the cross section for this process is  $<1\%$  of that of the photoelectric effect at a beam energy of 4 keV.

The limit of XBPM position resolution can be estimated as the uncertainty arising from the propagation of errors in equation (1). For the beam centered on the XBPM, thus generating equal signals and current noise on each quadrant, the limit of position resolution as determined by the noise is given by

$$\sigma_x = \frac{2\sigma I}{I_0} K_x, \quad (3)$$

where  $I_1 = I_2 = I_3 = I_4 = I_0/4$  is the electrode current and  $\sigma I = \sigma I_1 = \sigma I_2 = \sigma I_3 = \sigma I_4$  is the standard deviation of the measured currents.

As an illustration, consider a beam size of 500  $\mu\text{m}$  and  $E_{\text{ph}} = 4 \text{ keV}$ , and an incident flux of  $10^{12} \text{ photons s}^{-1}$  on a 3  $\mu\text{m}$ -thick diamond plate:  $3 \times 10^{10} \text{ photons s}^{-1}$  will be absorbed and, for our super-thin diamond plate, equations (1)–(3) predict a photocurrent of 1.9  $\mu\text{A}$ . In the limit where  $\sigma I \simeq 0.5 \text{ nA r.m.s.}$  is determined only by X-ray photon statistics, *i.e.* the shot noise (Spear, 2005), and with a scale factor  $K \simeq 0.25 \text{ mm}$ , we expect a position noise of  $\sim 125 \text{ nm r.m.s.}$  for a bandwidth of 100 Hz.

### 3. XBPM results and discussion

#### 3.1. XBPM fabrication

The diamond XBPM was mounted inside a dedicated ultra-high-vacuum (UHV) chamber on the SIRIUS beamline at SOLEIL. The XBPM was situated 3 m downstream of the channel-cut crystal X-ray monochromator at the beamline. The beam size of 0.5 mm (H)  $\times$  0.4 mm (V) at the XBPM was defined by collimator slits and verified with a YAG:Ce scin-

tillator beam viewer. The incident-beam flux was  $\sim 2 \times 10^{12}$  photons  $s^{-1}$  at 4 keV, as measured by a calibrated silicon photodiode placed just downstream of the XBPM. Unless otherwise indicated, all measurements described below were made with this configuration. Motorized translation stages enabled precise movement of the XBPM in two orthogonal directions ( $x, z$ ) transverse to the beam direction.

The rear-side contact of the XBPM was voltage biased and the current signals from the quadrant electrodes were measured by electrometer amplifiers (LOCuM-4, ENZ, <http://www.enz-de.de>) with the output voltages of the electrometers simultaneously digitized (Adlink ADC 2005, Adlink Technologie, <http://www.adlinktech.com>).

### 3.2. XBIC measurements

The X-ray beam induced currents (XBICs) and dark currents (*i.e.* with beam off) were measured for each quadrant as a function of the bias voltage, as shown in Fig. 3(a). At bias values greater than 6 V, corresponding to an applied electric field of  $2 \text{ V } \mu\text{m}^{-1}$ , with a constant-intensity beam on, the individual quadrant currents can be seen to all attain a plateau value of  $1.2 \mu\text{A}$ . The total diamond signal current was in good

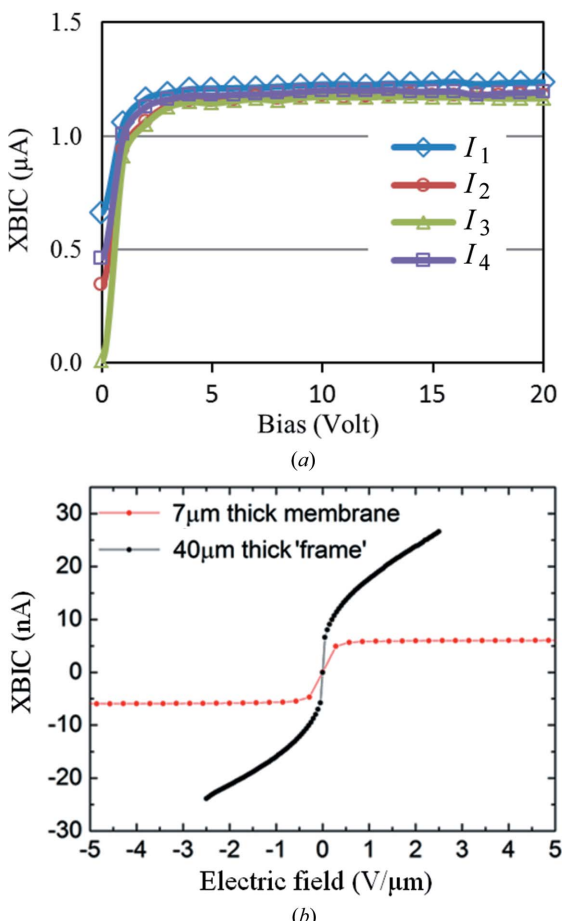


**Figure 3**

X-ray beam induced current (XBIC) *versus* detector bias for (a) the 3  $\mu\text{m}$ -thick membrane XBPM and (b) a diamond membrane detector fabricated earlier, showing the response of a 7  $\mu\text{m}$ -thick etched membrane with a 40  $\mu\text{m}$ -thick region surrounding the membrane.

agreement with the value predicted by equation (2), where we took a value of unity for the CCE, and with the value for the beam flux deduced from the calibrated silicon diode photocurrent. For an applied bias voltage of less than 20 V, the quadrant dark currents of the 3  $\mu\text{m}$  membrane XBPM were less than 1 pA (the precision here being limited by that of the electrometers), giving a signal-to-noise ratio, defined as the XBIC signal/leakage current noise, of greater than  $10^5$ .

The effect for  $\text{CCE} < 1$  is clearly shown in Fig. 3(b), which shows the beam-on  $I$ - $V$  response measured for a 7  $\mu\text{m}$ -thick membrane diamond that was processed earlier but using the same fabrication technique and grade of diamond material as for the 3  $\mu\text{m}$  membrane. Here, a plateau with  $\text{CCE} \simeq 1$  is reached for an applied field of  $0.5 \text{ V } \mu\text{m}^{-1}$ , whereas, for the 40  $\mu\text{m}$ -thick diamond surrounding the membrane,  $\text{CCE} < 1$  and still rising for applied fields  $> 2 \text{ V } \mu\text{m}^{-1}$  (the current measured in the thicker diamond was nevertheless higher due to the approximately sixfold higher beam absorption).

The phenomena of priming, *i.e.* an increase of measured signal current with steady-state time exposure of the diamond in the X-ray beam, and of signal lag, *i.e.* persistent currents measured after the beam is turned off, are well documented for pcCVD devices, and have also been observed in ‘hotspots’ corresponding to defective areas in some scCVD diamond XBPMs (Morse *et al.*, 2007; Bohon *et al.*, 2010). Fig. 4 shows a time scan of total current before and after the prompt opening

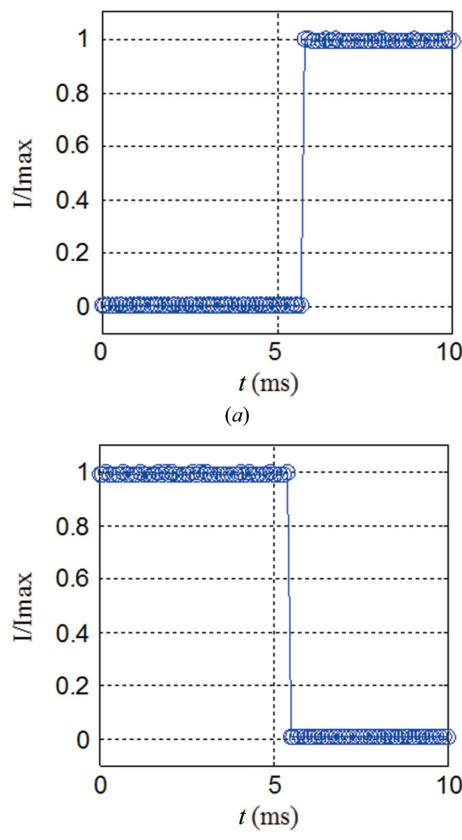


**Figure 4**

Time scan of XBIC as the X-ray beam shutter was (a) opened and (b) closed.

and closing of a shutter, confirming that, within the limits of precision of our measurements, both of these undesirable responses were absent with the super-thin XBPM tested here.

### 3.3. Position calibration of the XBPM

The beam positions in  $X$ ,  $Z$  are obtained using the difference or sum of the electrode currents as given by equation (1), but this also requires determination of scale factors  $K_x$ ,  $K_z$ . These calibration factors are, for a given beam size, simply determined by traversing the XBPM a known distance across the center of the beam. The plotted values of measured difference/sum currents *versus* position (Fig. 5) are linear regression fitted over the central region for both the horizontal  $X$  and vertical  $Z$  scans. In our case, this procedure gave scale factors of  $K_x = 0.29$  mm and  $K_z = 0.24$  mm, where the difference between the  $K$  values for the two orthogonal axes arises from the rectangular (because of the upstream collimator slits) shape of the beam.

To verify that the scale factors obtained were valid over an extended area around the center of the XBPM, an area scan was made, with the XBPM displaced in the beam at  $2.5\text{ }\mu\text{m}$  step intervals in  $X$  and  $Z$  using a collimated beam size reduced to  $50\text{ }\mu\text{m} \times 50\text{ }\mu\text{m}$ . The beam positions calculated according to equation (1) were compared with the actual scan positions, and the maximum position errors recorded were less than  $1\text{ }\mu\text{m}$  at all positions within the bounds of the mapped area, which was a square of size  $1\text{ mm}^2$ .

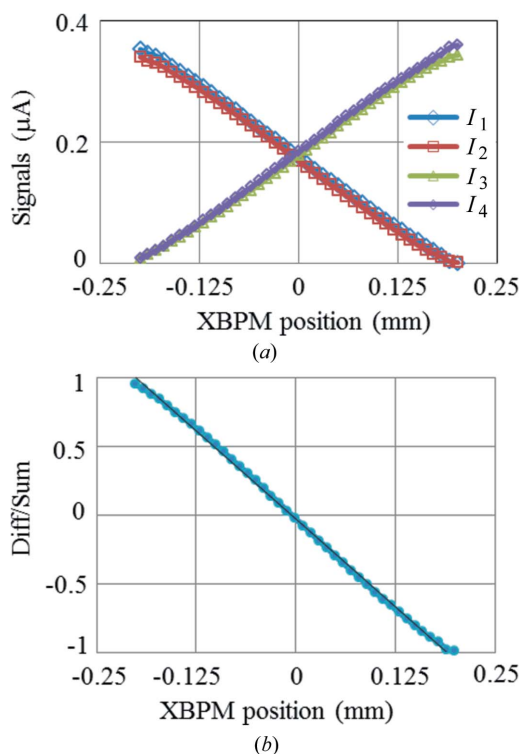


**Figure 5**  
(a) Measured quadrant currents *versus* XBPM displacement through the beam in a vertical direction. (b) Corresponding calculated difference/sum currents *versus* XBPM displacement in a vertical direction.

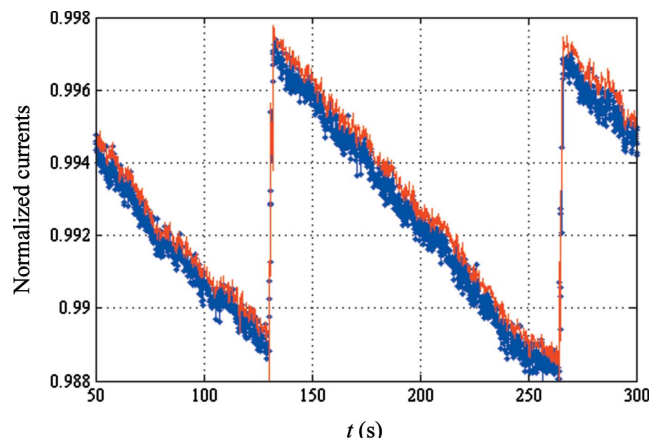


**Figure 6**  
Time scan showing the top-up mode of operation of the SOLEIL synchrotron: scCVD diamond XBPM (blue) and the corresponding downstream Si photodiode (red) current signals.

### 3.4. Diamond intensity tracking

The diamond membrane XBPM demonstrated precise measurement of the beam intensity with a current noise of  $0.5\text{ nA r.m.s.}$ , corresponding to  $0.02\%$  of the signal intensity for the measurement conditions specified in §2.2. Fig. 6 is a time scan of the total beam intensity, comparing the response (total current) of the diamond XBPM with that of the downstream silicon photodiode. The sawtooth traces correspond to the ‘top-up’ operation mode of the SOLEIL synchrotron storage ring, involving re-injections every four minutes, which raise the stored synchrotron current by  $0.5\%$ . Within the accuracy of the data point-to-point measurement noise, both the silicon and diamond devices clearly track the varying beam intensity in an identical manner.

### 3.5. XBPM response homogeneity

The area scan map referred to in §3.3 enabled us to investigate the inhomogeneity of the diamond XBPM response. The total current ( $I_0$ ) map over  $1\text{ mm}^2$  is shown in Fig. 7 and reveals a relative intensity variation of  $\sim 50\%$  as a left-to-right variation. In the central  $200\text{ }\mu\text{m} \times 200\text{ }\mu\text{m}$  area we measured a more reasonable peak-to-peak signal variation of  $0.6\text{ }\mu\text{A}$  around the mean value of  $5\text{ }\mu\text{A}$ , *i.e.* a  $12\%$  variation. Note, however, that there is no evidence of smaller scale response variations arising from local defects. We are confident that this ‘wedge’ spatial response variation is attributable simply to variation in the total thickness of the diamond plate before the Ar-O etching-thinning process was carried out, as optical measurement of the variation in the total thickness of a previous diamond plate that had been scaife polished by DDK to  $40\text{ }\mu\text{m}$  thickness showed a similar extent of ‘wedge’ error thickness. This non-uniformity of response is a significant limitation of the present device. However, since the time of these measurements, we have verified that thinned plates can be obtained from an alternative supplier with total thickness variation held within  $1\text{ }\mu\text{m}$ , by using a modified scaife polishing process.

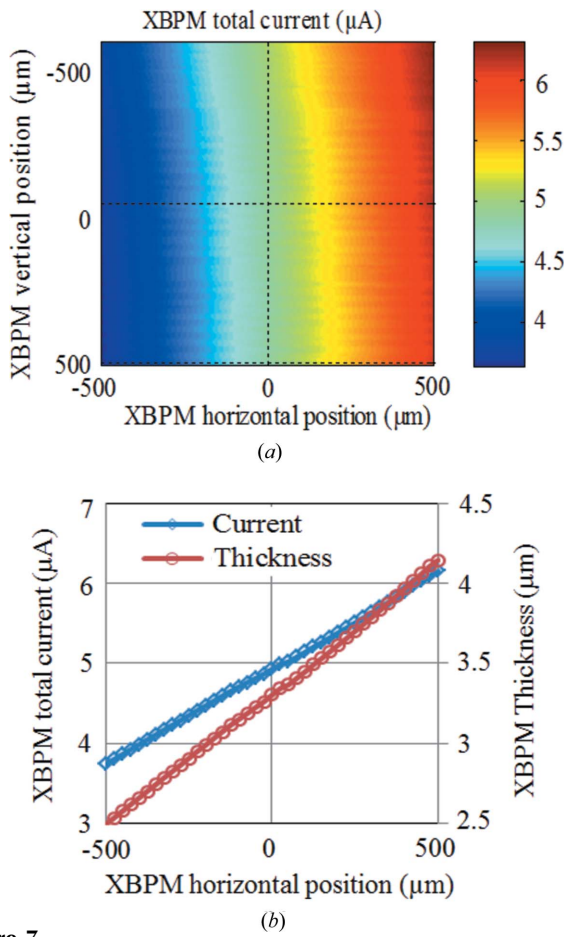


**Figure 7**

(a) Total current  $I_0$  map made over the central area of the diamond XBPM, and (b) the corresponding intensity and XBPM thickness profile measured along the  $X$  axis.

### 3.6. XBPM responsivity

For low-energy X-ray beams for which the Compton and elastic scattering cross sections may be considered as negligible, the XBPM can easily be calibrated with reference to a silicon diode for use as an absolute beam flux monitor. As a demonstration of this, the total current of the diamond XBPM was recorded as the beamline monochromator was scanned over the energy range 1.4–4.5 keV, while at the same time measuring the current from the calibrated silicon photodiode. The measured XBPM responsivity is shown in Fig. 8, together with the theoretical responsivity curve as given by equation (2) where we have used a mean diamond thickness  $L = 3 \mu\text{m}$ , CCE = 1 and  $\varepsilon_p = 13.25 \text{ eV}$ .

### 3.7. XBPM spatial resolution

We define here the spatial resolution of the detector to be the smallest position variation of the beam which can be measured by the XBPM for a given signal integration time. This spatial resolution can be estimated in two ways:

(i) Directly, by scanning the XBPM across to the beam and comparing the XBPM calculated positions with those reported

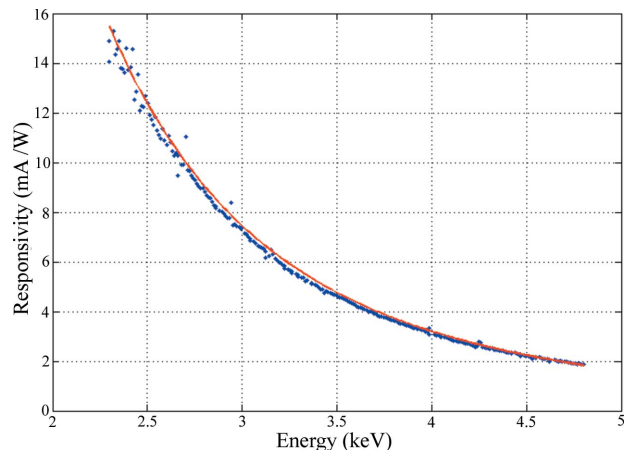


**Figure 8**

The super-thin diamond XBPM responsivity *versus* X-ray beam energy. The measured experimental points (in blue) are compared with the theoretical response predicted by equation (2).

by the scan motors. This requires deconvolution of the noise associated with the motor movements.

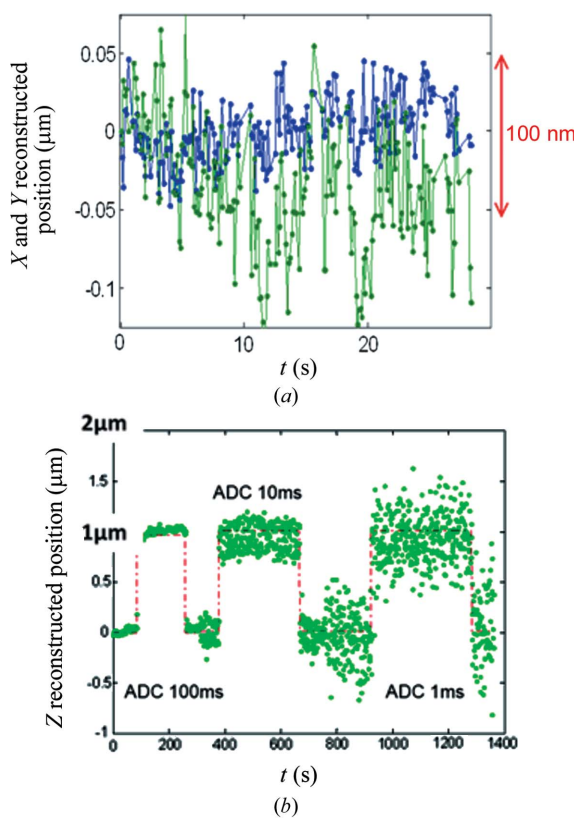
(ii) Indirectly, with the XBPM in a fixed position, by measuring the successive point-to-point variations in the XBPM calculated positions in a time scan.

Both of these methods give a worst-case value, as the measured data are necessarily convoluted with real movements of the X-ray beam as the measurements are made.

A measurement of position noise with the detector kept at a fixed position is given by the time scan in Fig. 9(a), shown here for a signal integration time equal to the sampling interval of 100 ms. The standard deviation of the calculated XBPM positions obtained with integration times of 100, 10 and 1 ms were, respectively, 20, 120 and 250 nm for the  $x$  (horizontal) axis, and 40, 250 and 800 nm for the  $z$  (vertical) axis. The position resolution for these sampling times is also illustrated in Fig. 9(b), where the XBPM vertical position has been stepped by 1  $\mu\text{m}$  between the measurements made with 100, 10 and 1 ms integration times.

### 4. Conclusion

We have fabricated and characterized a highly transmissive super-thin membrane XBPM made from a low-cost grade of scCVD diamond. With such a device we obtained submicrometer position resolution, similar to that previously observed only with high-purity scCVD diamond plates of a thickness which results in an unacceptable level of beam absorption for use in X-ray beams of less than 5 keV. These super-thin membrane scCVD diamond XBPMs are promising for instrumentation of soft and tender X-ray beamlines: they demonstrate time-stable operation, with no evidence of priming nor persistent signal lag effects; they are homogeneous in their response, and beam monitoring with submicrometer position resolution was demonstrated with only  $\sim 3\%$  absorption of incident beam at 4 keV. Following its initial characterization as described above, this XBPM has

**Figure 9**

(a) Time scan of the beam reconstructed position in horizontal and vertical directions with 100 ms XBPM signal integrations. (b) Time scan made with 1  $\mu\text{m}$  XBPM positions steps and integration times of 100, 10 and 1 ms.

been installed for one year and used during all the commissioning of the SOLEIL synchrotron SIRIUS beamline; during this time it has shown no evidence of radiation damage or other deterioration. The fabrication of a new series of such devices is now in progress, for which the non-uniformity in response due to the wedge thickness variation of the diamond plate will be reduced by a factor of five or more.

The authors thank the SIRIUS and SIXS beamline teams for their support and the beam time necessary for the characterization of the XBPM.

## References

- Alkire, R. W., Rosenbaum, G. & Evans, G. (2000). *J. Synchrotron Rad.* **7**, 61–68.
- Berdermann, E. *et al.* (2010). *Diamond Relat. Mater.* **19**, 358–367.
- Bergonzo, P., Brambilla, A., Tromson, D., Marshall, R. D., Jany, C., Foulon, F., Gauthier, C., Solé, V. A., Rogalev, A. & Goulon, J. (1999). *J. Synchrotron Rad.* **6**, 1–5.
- Bohon, J., Muller, E. & Smedley, J. (2010). *J. Synchrotron Rad.* **17**, 711–718.
- Desjardins, K., Duran, D., Hustache, S., Pomorski, M. & Shepard, W. (2013). *J. Phys. Conf. Ser.* **425**, 212004.
- Fuchs, M. R., Holldack, K., Reichardt, G. & Mueller, U. (2007). *AIP Conf. Proc.* **879**, 1006–1009.
- Isberg, J., Hammersberg, J., Johansson, E., Wikström, T., Twitchen, D. J., Whitehead, A. J., Coe, S. E. & Scarsbrook, G. A. (2002). *Science*, **297**, 1670–1672.
- Kazovsky, L. G. (1983). *Opt. Eng.* **22**, 339–347.
- Keister, J. W. & Smedley, J. (2009). *Nucl. Instrum. Methods Phys. Res. A*, **606**, 774–779.
- Medjoubi, K., Leclercq, N., Langlois, F., Buteau, A., Lé, S., Poirier, S., Mercère, P., Sforza, M. C., Kewish, C. M. & Somogyi, A. (2013). *J. Synchrotron Rad.* **20**, 293–299.
- Morse, J., Salomé, M., Berdermann, E., Pomorski, M., Cunningham, W. & Grant, J. (2007). *Diamond Relat. Mater.* **16**, 1049–1052.
- Morse, J., Solar, B. & Graafsma, H. (2010). *J. Synchrotron Rad.* **17**, 456–464.
- Muller, E. M., Smedley, J., Bohon, J., Yang, X., Gaowei, M., Skinner, J., De Geronimo, G., Sullivan, M., Allaire, M., Keister, J. W., Berman, L. & Héroux, A. (2012). *J. Synchrotron Rad.* **19**, 381–387.
- Pomorski, M., Berdermann, E., de Boer, W., Furgeri, A., Sander, C. & Morse, J. (2007). *Diamond Relat. Mater.* **16**, 1066–1069.
- Pomorski, M., Caylar, B. & Bergonzo, P. (2013). *Appl. Phys. Lett.* **103**, 112106.
- Schildkamp, W. & Pradervand, C. (1995). *Rev. Sci. Instrum.* **66**, 1956–1959.
- Silhout, R. van, Kachatkou, A., Kyele, N., Scott, P., Martin, T. & Nikitenko, S. (2011). *Opt. Lett.* **36**, 570–572.
- Somogyi, A., Kewish, C. M., Polack, F. & Moreno, T. (2011). *AIP Conf. Proc.* **1365**, 57–60.
- Spear, J. D. (2005). *Rev. Sci. Instrum.* **76**, 076101.